Engineering and Laboratory Note Vol. 57, No. 13 / 1 May 2018 / *Applied Optics* 3401

applied optics

Analysis and correction for measurement error of edge sensors caused by deformation of guide flexure applied in the Thirty Meter Telescope SSA

HAIFENG CAO,[1,2,3] JINGXU ZHANG,[1,4] FEI YANG,[1,*] QICHANG AN,[1,2,5] HONGCHAO ZHAO,[1,6] AND PENG GUO[1,2,7]

[1]*Changchun Institute of Optics, Fine Mechanics and Physics, Chinese Academy of Sciences, Changchun 130033, China*
[2]*University of Chinese Academy of Sciences, Beijing 100039, China*
[3]*e-mail: caohf_ucas@163.com*
[4]*e-mail: Zhangjx@ciomp.ac.cn*
[5]*e-mail: anjj@mail.ustc.edu.cn*
[6]*e-mail: zhaohcciomp@163.com*
[7]*e-mail: guopengmse@gmail.com*
**Corresponding author: yangf@ciomp.ac.cn*

Received 8 December 2017; revised 12 March 2018; accepted 23 March 2018; posted 26 March 2018 (Doc. ID 314390); published 25 April 2018

The Thirty Meter Telescope (TMT) project will design and build a 30-m-diameter telescope for research in astronomy in visible and infrared wavelengths. The primary mirror of TMT is made up of 492 hexagonal mirror segments under active control. The highly segmented primary mirror will utilize edge sensors to align and stabilize the relative piston, tip, and tilt degrees of segments. The support system assembly (SSA) of the segmented mirror utilizes a guide flexure to decouple the axial support and lateral support, while its deformation will cause measurement error of the edge sensor. We have analyzed the theoretical relationship between the segment movement and the measurement value of the edge sensor. Further, we have proposed an error correction method with a matrix. The correction process and the simulation results of the edge sensor will be described in this paper.

OCIS codes: (010.1080) Active or adaptive optics; (110.6770) Telescopes; (120.5050) Phase measurement; (130.6010) Sensors; (150.1488) Calibration.

https://doi.org/10.1364/AO.57.003401

1. INTRODUCTION

The largest diameter of monolithic optical telescopes is approximately 8 m [1], which has reached the limit of its design and manufacture. Larger telescopes require the primary mirror to be segmented. To form a coherent image, the individual segments of the primary mirror need to be kept phased, because changes in wind load, vibration, heat, and the direction of gravity will affect the relative positions of segments [2–7]. This is achieved by a control system, which takes sensor readings and then feeds back commands to a set of actuators that control the position of the individual segments.

There are a number of different sensor types that can be used in this servo loop [8–16]. Edge sensors can measure the relative height and possible gap or shear between adjacent segments. These sensors have appeared on a number of existing telescopes and are the baseline of the next generation giant segmented mirror telescopes (GSMT) [17,18].

The Thirty Meter Telescope (TMT) project, a partnership among America, China, Japan, Canada, and India, is currently developing a 30-m-diameter segmented optical telescope. The primary mirror of TMT is an array of 492 nearly identical hexagonal mirror segments, nominally separated by 2.5 mm gaps [19]. The primary mirror support system (PMSS) holds these 492 segments in position, allowing the array to work as a single mirror. The passive support system supports each mirror segment and controls its rotation in the mirror plane. The active control system (ACS) controls the tip, tilt, and piston of each segment relative to the other segments. The ACS utilizes edge sensors on the back of the segments to measure their relative positions and to control electronics hardware and software to interpret the position data and actuators to move the segments as commanded [20].

The surface of the primary mirror is an ellipsoid of reflection, and the surface of each mirror segment is an off-axis portion of that surface. The size and prism shape of the segments vary slightly [21], depending on their position in the array.

The rest of this paper is organized as follows. Section 2 presents the structure design and layout of edge sensors used in TMT. In Section 3, a kinematic model of the segment mirror system is introduced based on the analysis of structural error. In Section 4, simulation experiments are investigated to check the performance of the model and error correction method. In Section 5, simulation experiments are carried out to verify the ability of this method in correcting the measurement error caused by the tip and tilt of the segmented mirror. Section 6 concludes the paper.

2. DEFINITIONS AND ANALYSIS

A. Geometric Layout of Edge Sensors

The TMT edge sensor is a capacitive displacement sensor, as shown in Fig. 1 [17], which is fixed below the edge of the submirror; the board and the mirror are arranged vertically [17].

As shown in Fig. 1, each drive plate area is $A_0 = \omega l/2$. Assuming that the vertical spacing between the plates is small, the geometric layout shown in Fig. 2 is still applicable, but $g = 0$.

B. Analysis

Provided that the segments have been adjusted to achieve optical confocal/co-phase, the capacitance of each sensor can be calculated from the formula [24]

$$C_0 = \varepsilon \frac{A_0}{d_0}, \tag{1}$$

where ε is the permittivity of the dielectric, A_0 is the area of overlap of the plates, and d_0 is the distance between the plates.

As one segment moves up by an amount of Δs relative to its neighbor, the changes in the area of the upper and lower drive plates are ΔA_1 and ΔA_2, respectively, and the differential capacitance will change according to

$$\Delta C_1 = \varepsilon \frac{A_0 + \Delta A_1}{d_0 + \Delta d_1} - \varepsilon \frac{A_0}{d_0}, \tag{2}$$

$$\Delta C_2 = \varepsilon \frac{A_0 + \Delta A_2}{d_0 + \Delta d_2} - \varepsilon \frac{A_0}{d_0}, \tag{3}$$

$$\frac{\Delta C_1 - \Delta C_2}{C_0} = \frac{A_0(\Delta d_2 - \Delta d_1) + d_0(\Delta A_1 - \Delta A_2)}{d_0 + \Delta d_1 + \Delta d_2 + \Delta d_1 \Delta d_2 / d_0} \frac{1}{A_0}. \tag{4}$$

In Eqs. (2)–(44), Δd_1 and Δd_2 are the distance changes between the plates in the upper and lower capacitors. There is a symmetry based on the upper and lower drive plate structures:

$$\Delta d_1 + \Delta d_2 = 0. \tag{5}$$

Considering Δd_1 and Δd_2 are small compared with d_0, that is

$$\frac{\Delta d_1 \Delta d_2}{d_0} = 0. \tag{6}$$

Equation (4) is further simplified as

$$\frac{\Delta C_1 - \Delta C_2}{C_0} = \frac{\Delta A_1 - \Delta A_2}{A_0} + \frac{\Delta d_2 - \Delta d_1}{d_0}. \tag{7}$$

The first and second terms on the right-hand side of Eq. (7) are caused by the shear and rotation of the segment relative to its neighbor across the gap, respectively, e.g., the change in the dihedral angle. Similarly, in order to simplify the discussion of the problem, assuming that the size of all the edge sensor structures is the same, we installed the drive plate (two plates) in even position and the sense board (one plate) in odd position, as shown in Fig. 2.

We suppose the segment is a regular hexagon, and we only consider the change of sensor No. 11 when actuator P_B is pistoned out of the page by Δz. In this case, Eq. (7) reduces to

$$\frac{\Delta C_1 - \Delta C_2}{C_0} = \frac{4r\Delta z}{hl} - \frac{l\Delta z}{2dh}. \tag{8}$$

The first term on the right-hand side of Eq. (8) is dependent on the overlap area. The second is affected by the change in the effective spacing of the plates.

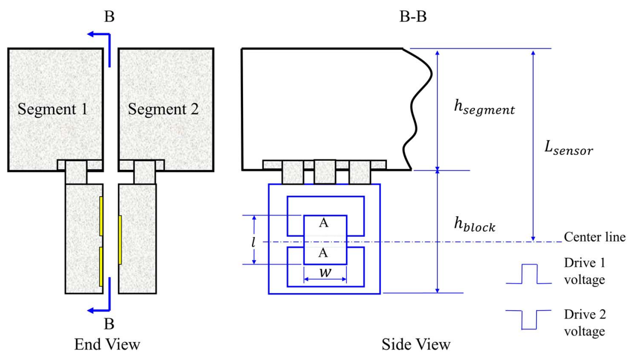

Fig. 1. Sensor geometry of TMT; ω and l represent the width and height of the drive plate, respectively.

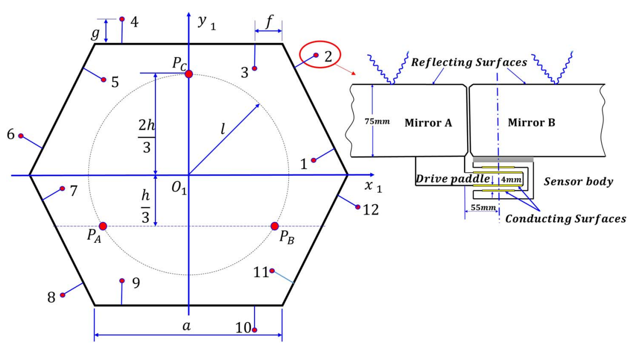

Fig. 2. Geometric layout of edge sensors and displacement actuators in segmented mirror of Keck [22,23].

3. MEASUREMENT ERROR ANALYSIS

A. Creating Coordinate System

The support system assembly (SSA) of the segmented mirror determines that its instant center is not the center of the mirror but the center of the guide flexure. Actually, it will bring in error because the instant center of the segmented mirror changes when its position changes. Here, we call it "structural error."

In this paper, the SSA model is constructed and the spatial pose of the drive plate relative to the sense plate is obtained by means of coordinate transformation. The relationship between the sensor reading and the three displacement actuators is calculated, and the corresponding correction coefficient is

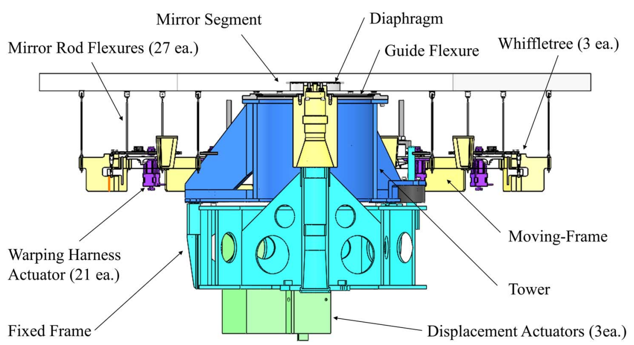

Fig. 3. Schematic diagram of the TMT primary mirror segment and support system.

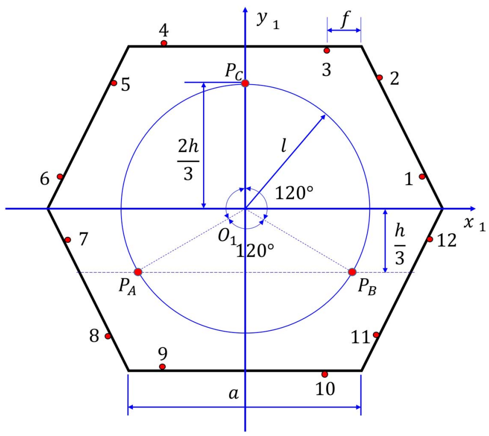

Fig. 5. Establishment of coordinate system (CS).

given in the latter part. The geometrical structure and three-dimensional model of the sub-mirror are shown in Fig. 3.

The moving frame and tower are connected by the guide flexure to limit the three DOFs (rotating along the z axis, moving along the x/y axis) of the segmented mirror. The remaining three DOFs (tip, tilt, and piston) are determined by the three actuators. According to the kinematics theory of the mechanism, the number of the driving links (P_A, P_B, P_C) of the mechanism is 3, and the degree of freedom of the mechanism is also 3.

The number of DOFs of the mechanism is equal to the number of driving links, so the movement of the mechanism is determined. Thus, the spatial position of the segmented mirror can be determined by controlling the output of the three displacement actuators. The simplified multi-body kinematics model is shown in Fig. 4.

The guide flexure is simplified as the composite hinge model of the spherical hinge and the prismatic hinge in the multi-body kinematics, the actuator displacement output mechanism is simplified as a cylindrical hinge, and the flexible rods for displacement output are fixed with the moving frame. The flexible rods only have the freedom of vertical movement. In order to meet the compatibility requirements of the hinges, the other DOFs are released.

As shown in Fig. 5, it is assumed that the center of the ball hinge is the origin O_1 after the optical co-phase adjustment. The direction starting from O_1, parallel to $\overrightarrow{P_AP_B}$ and pointing to P_B, is defined as the x axis. The direction of the y axis is the same with $\overrightarrow{O_1P_C}$ while the direction of the z axis meets the right-hand rule. Then the coordinate system $O_1 - x_1y_1z_1$ is established.

The TMT sensors are perpendicular; that is, the plates of the different capacitors that make up the sensors are perpendicular to the segment surface, as shown in Fig. 6. The geometric relationships between the 12 half-sensors and the segmented mirror are depicted in Fig. 2, from which the placement of the three segment actuators is also indicated. The Keck parameters are given by $a = 900$ mm, $f = 173$ mm, $g = 55$ mm, and $h = 706$ mm [22]. The TMT parameters are given by $a = 717$ mm [25] (we just rounded it up to 720 mm), $g = 0$, $d = 2$ mm, and $f = 717 \times 173/900$ mm ≈ 138 mm.

The original coordinates of the three points (P_A, P_B, P_C) in the coordinate system $O_1 - x_1y_1z_1$ are defined as $P_A(-l\cos 30°, -l\sin 30°, -m)$, $P_B(l\cos 30°, -l\sin 30°, -m)$, and $P_C(0, l, -m)$.

Assume that the output displacements of the three actuators (A, B, and C) are Δa, Δb, and Δc, respectively. The position and posture of the segmented mirror can be described by the Euler angle; that is, it is equivalent to the segment moving t along the z axis, rotating α along the x axis, and rotating β along the new y axis of the conjoined coordinate system [26]. The corresponding homogeneous coordinate transformation matrices are defined as

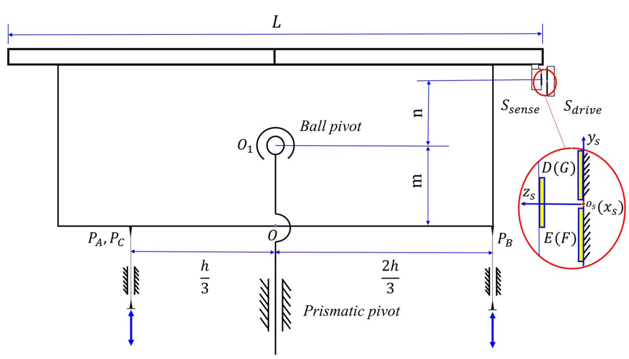

Fig. 4. Kinematic model of segment mirror system.

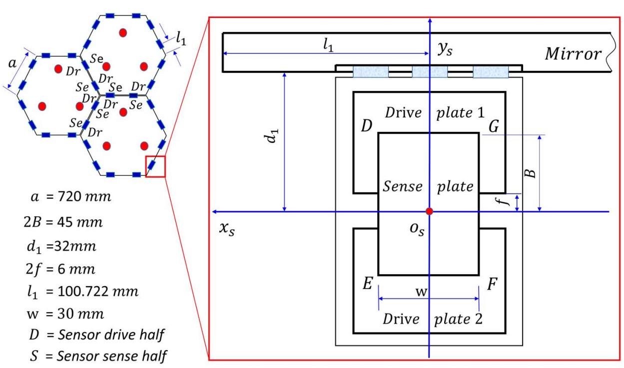

Fig. 6. Dimensions of capacitor plate in millimeters [17].

$$\mathrm{Trans}(0,0,t)=\begin{bmatrix}1&0&0&0\\0&1&0&0\\0&0&1&t\\0&0&0&1\end{bmatrix},$$

$$\mathrm{Rot}(X,\alpha)=\begin{bmatrix}1&0&0&0\\0&\cos\alpha&-\sin\alpha&0\\0&\sin\alpha&\cos\alpha&0\\0&0&0&1\end{bmatrix},$$

$$\mathrm{Rot}(Y,\beta)=\begin{bmatrix}\cos\beta&0&\sin\beta&0\\0&1&0&0\\-\sin\beta&0&\cos\beta&0\\0&0&0&1\end{bmatrix}. \tag{9}$$

The coordinates of $P_i(i=A,B,C)$ after moving are $P_i'(i=A,B,C)$, which can be expressed as

$$\begin{aligned}[P_A' \quad P_B' \quad P_C'] &= \mathrm{Rot}(Y,\beta)\mathrm{Rot}(X,\alpha)\mathrm{Trans}(0,0,t)\\ &\quad *[P_A \quad P_B \quad P_C]\\ &= T[P_A \quad P_B \quad P_C].\end{aligned} \tag{10}$$

Thus Eq. (10) can be rearranged as

$$\begin{cases}-m+\Delta a=\sqrt{3}l\sin\beta/2+(t-m)\cos\alpha\cos\beta\\ -l\sin\alpha\cos\beta/2\\ -m+\Delta b=(t-m)\cos\alpha\cos\beta-\sqrt{3}l\sin\beta/2\\ -l\sin\alpha\cos\beta/2\\ -m+\Delta c=(t-m)\cos\alpha\cos\beta+l\sin\alpha\cos\beta\end{cases}. \tag{11}$$

Considering α, β are small, we can get $\sin\alpha=\alpha$, $\sin\beta=\beta$, and $\cos\alpha=1$, $\cos\beta=1$. Substituting it into Eq. (11), we have the following relationship:

$$\begin{cases}\Delta a=\sqrt{3}l\beta/2+t-l\alpha/2\\ \Delta b=t-\sqrt{3}l\beta/2-l\alpha/2\\ \Delta c=t+l\alpha\end{cases}, \tag{12}$$

$$\begin{cases}t=(\Delta a+\Delta b+\Delta c)/3\\ \alpha=-(\Delta a+\Delta b-2\Delta c)/3l\\ \beta=\sqrt{3}(\Delta a-\Delta b)/3l\end{cases}. \tag{13}$$

The coordinates of the four vertices D, E, F, and G on the sense plate in the world coordinate system (WCS) are P_D', P_E', P_F', and P_G':

$$[P_D' \quad P_E' \quad P_F' \quad P_G'] = T[P_D \quad P_E \quad P_F \quad P_G]. \tag{14}$$

B. Coordinate Transformation

Assuming that the position vector of the point P is ${}^AP$ in the coordinate system {A}, the position vector of the point P is ${}^BP$ in the coordinate system {B}, the position and pose matrix of CS {B} is ${}^AR_B$ in the CS {A}, the position vector of the origin in CS {B} is ${}^AP_B$ in the CS {A}, and the relationship of them is given by [27]

$${}^AP={}^AR_B{}^BP+{}^AP_B, \tag{15}$$

$${}^BP={}^AR_B^{-1}({}^AP-{}^AP_B), \tag{16}$$

$${}^AP=P_{i'}(i=D,E,F,G), \tag{17}$$

where

$${}^AP_B=(x_B^A,y_B^A,z_B^A). \tag{18}$$

${}^AR_B$ can be obtained by coordinate transformation. The CS {B} can be regarded as the CS {A} translating along the vector ${}^AP_B$, then rotating by 240° along the z axis, then rotating by 90° along the x axis; that is,

$${}^AR_B=R(Z,240°)R(X,90°)=\begin{bmatrix}-1/2&0&-\sqrt{3}/2\\-\sqrt{3}/2&0&1/2\\0&1&0\end{bmatrix}, \tag{19}$$

$${}^AR_B^{-1}=\begin{bmatrix}-1/2&0&-\sqrt{3}/2\\-\sqrt{3}/2&0&1/2\\0&1&0\end{bmatrix}^{-1}=\begin{bmatrix}-1/2&-\sqrt{3}/2&0\\0&0&1\\-\sqrt{3}/2&1/2&0\end{bmatrix}. \tag{20}$$

As shown in Fig. 7, the coordinates of D, E, F, and G in the CS of the drive plate are $D(x_D,y_D,z_D)$, $E(x_E,y_E,z_E)$, $F(x_F,y_F,z_F)$, and $G(x_G,y_G,z_G)$.

The projection coordinates of D, E, F, and G on the plane of $x_so_sy_s$ in the drive plate coordinate system are $D'(x_D,y_D)$, $E'(x_E,y_E)$, $F'(x_F,y_F)$, and $G'(x_G,y_G)$, respectively.

The plane can be obtained by the coordinates of D, E, and F, and its expression is given by

$$A_px+B_py+C_pz+D_p=0, \tag{21}$$

where the coefficients of the plane equation above are given by

$$\begin{vmatrix}x&y&z&1\\x_D&y_D&z_D&1\\x_E&y_E&z_E&1\\x_F&y_F&z_F&1\end{vmatrix}=0. \tag{22}$$

Let θ be the dihedral angle of the plane DEFG and the plane of $x_so_sy_s$:

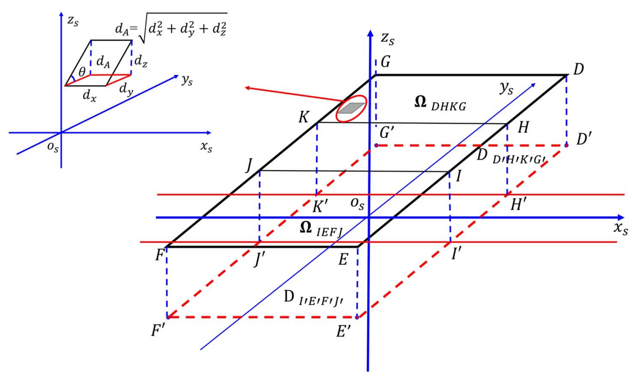

Fig. 7. Coordinates of DEFG in CS $\{o_s-x_sy_sz_s\}$.

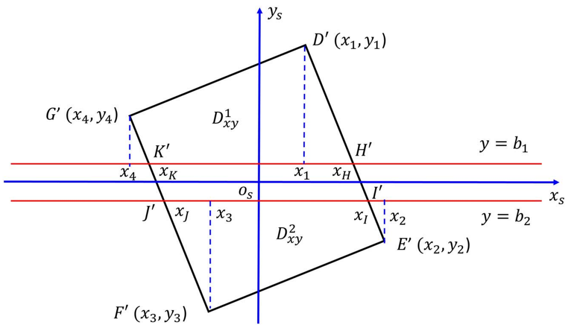

Fig. 8. Projection area of the sense plate on the plane of drive plates.

$$\cos\,\theta = \frac{|A_p \cdot 0 + B_p \cdot 0 + C_p \cdot 1|}{\sqrt{A_p^2 + B_p^2 + C_p^2}\sqrt{0^2 + 0^2 + 1^2}} = \frac{|C_p|}{\sqrt{A_p^2 + B_p^2 + C_p^2}}. \tag{23}$$

We give a calculation Eq. (24) for capacitance integral by Eq. (8) as follows:

$$\begin{aligned} C &= \varepsilon \iint_\Omega \frac{\mathrm{d}_A \cos\,\theta}{z} = \varepsilon \cos\,\theta \iint_\Omega \frac{\mathrm{d}_A}{z} \\ &= \varepsilon \cos\,\theta \iint_{Dxy} \sqrt{1 + z_x^2 + z_y^2}\, \frac{1}{z(x,y)} \mathrm{d}_x \mathrm{d}_y \\ &= -\varepsilon C_p \iint_{Dxy} \frac{1}{A_p x + B_p y + D_p} \mathrm{d}_x \mathrm{d}_y, \end{aligned} \tag{24}$$

where D_{xy} (D^1_{xy} and D^2_{xy}) are the two regions of the geometric pattern surrounded by DEFG on the plane $x_s o_s y_s$ and separated by $y = b_1$ and $y = b_2$, as shown in Fig. 8.

C_{static} is the capacitance of the upper and lower capacitors when the segmented mirror is calibrated by the actuators, and we assume that the space between the drive plates and the sense plate is d_{static}; then we get

$$C_{\text{static}} = \varepsilon \frac{A_{\text{static}}}{d_{\text{static}}}, \tag{25}$$

$$\begin{aligned} C_1 &= C_{\text{UP}} = -\varepsilon C_p \iint_{D^1 xy} \frac{1}{A_p x + B_p y + D_p} \mathrm{d}_x \mathrm{d}_y, \\ C_2 &= C_{\text{DOWN}} = -\varepsilon C_p \iint_{D^2 xy} \frac{1}{A_p x + B_p y + D_p} \mathrm{d}_x \mathrm{d}_y \\ \frac{\Delta C_1 - \Delta C_2}{C_{\text{static}}} &= \frac{C_{\text{UP}} - C_{\text{DOWN}}}{C_{\text{static}}} \\ &= \frac{\varepsilon C_p}{C_{\text{static}}} \left(\begin{array}{l} -\iint_{D^1 xy} \frac{1}{A_p x + B_p y + D_p} \mathrm{d}_x \mathrm{d}_y \\ +\iint_{D^2 xy} \frac{1}{A_p x + B_p y + D_p} \mathrm{d}_x \mathrm{d}_y \end{array} \right). \end{aligned} \tag{26}$$

C. Numerical Calculation

A code was developed under MATLAB programming environment for numerical calculation to find the relationships between the output displacements Δa, Δb, Δc by actuators A, B, and C and $(\Delta C_1 - \Delta C_2)/C_0$ denoted by ζ.

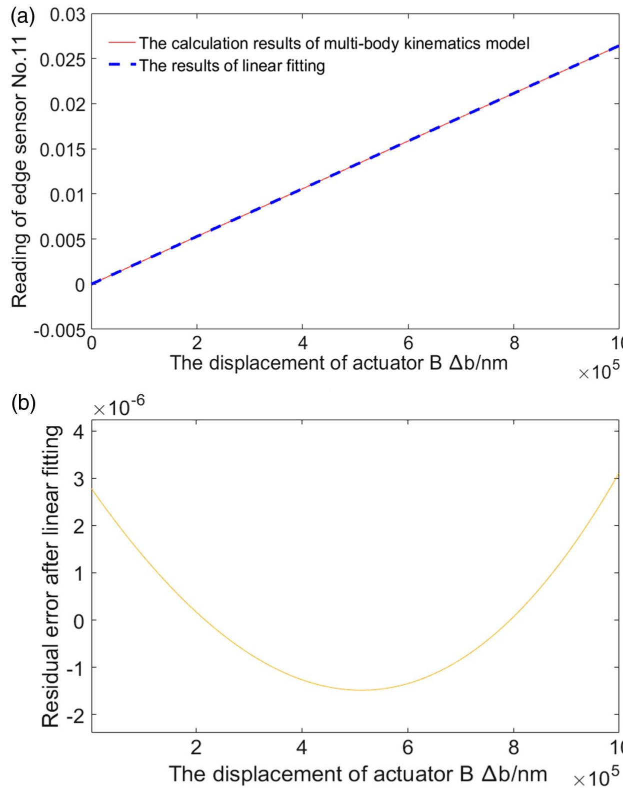

Fig. 9. Relationship between input (Δb) and output (ζ) in the case of $\Delta a = \Delta c = 0$: (a) Reading of edge sensor No. 11. (b) Residual error after fitting.

First, we consider what the relationship between input (Δb) and output (ζ) is in the case of $\Delta a = \Delta c = 0$. The displacement Δb ranges from 0 to 1 mm, and the step length is 1 μm, as shown in Fig. 9(a).

It can be seen from Figs. 9(a) and 9(b) that the relationship between the edge sensor reading and the displacement of the actuators is almost linear, not absolutely linear, but it will be regarded as a linear process in the practical application [28], which is

$$\sum_{i,j} a_{i,j} P_{i,j} \qquad (i = 1, 2; j = 1, 2, 3), \tag{27}$$

where i is the number of two adjacent segmented mirrors, j is the number of actuators fixed on the mirror, and $a_{i,j}$ denotes the corresponding coefficient.

For the edge sensor processing circuit, there is a certain error in the actual value calculated according to Eq. (27). The result of the linear fitting of Eq. (26) is

$$\zeta = 6.2869 \times 10^{-8} \Delta b - 2.4573 \times 10^{-7}. \tag{28}$$

The absolute value of the maximum residual error is 4.813×10^{-6}.

The result calculated according to Eq. (8) is

$$\Delta b' = \frac{\xi}{\frac{4}{l} - \frac{l}{2hd}}. \tag{29}$$

Thus the absolute error is

$$\Delta b - \Delta b' = \Delta b - \frac{\xi}{\frac{4}{l} - \frac{l}{2hd}}. \tag{30}$$

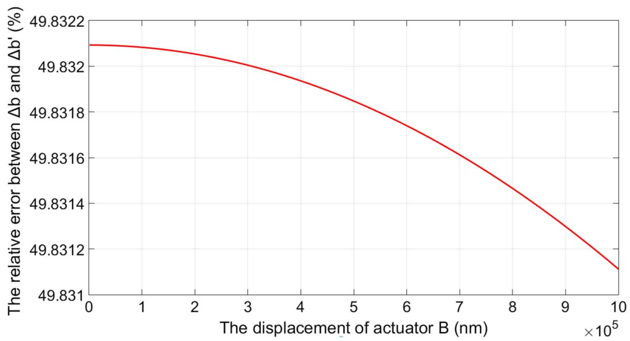

Fig. 10. Trend graph of relative error between Δb and $\Delta b'$.

And the relative error is

$$\left|\frac{\Delta b - \Delta b'}{\Delta b}\right| \times 100\%. \quad (31)$$

The relative error curve is shown as Fig. 10, from which we can get the following conclusion:

$$49.83\% < \left|\frac{\Delta b - \Delta b'}{\Delta b}\right| \times 100\% < 49.84\%. \quad (32)$$

4. ERROR CORRECTION AND SIMULATION

A. Error Correction Method

The relative error value is stable, which is beneficial to the correction of error caused by the structure error.

In the case of Δa and Δc being determined, the true value Δb is a function of the measured value $\Delta b'$, which is expressed as a polynomial:

$$\Delta b = \sum \omega_1 \Delta b' + \omega_2 \Delta b'^2 + \omega_3 \Delta b'^3 + \cdots. \quad (33)$$

In Eq. (33), ω_i is also related to the value of Δa and Δc. $\omega_i = \omega_i(\Delta a, \Delta c) = \sum k + k\Delta a + k\Delta a^2 + k\Delta a^3 + \cdots + k\Delta c + k\Delta c^2 + k\Delta c^3 + \cdots$. We take the 7×4 order matrix for fitting, which can be expressed by

$$\Delta b = [1 \quad \Delta a \quad \Delta a^2 \quad \Delta a^3 \quad \Delta c \quad \Delta c^2 \quad \Delta c^3] * \begin{bmatrix} k_{11} & k_{12} & k_{13} & k_{14} \\ k_{21} & k_{22} & k_{23} & k_{24} \\ k_{31} & k_{32} & k_{33} & k_{34} \\ k_{41} & k_{42} & k_{43} & k_{44} \\ k_{51} & k_{52} & k_{53} & k_{54} \\ k_{61} & k_{62} & k_{63} & k_{64} \\ k_{71} & k_{72} & k_{73} & k_{74} \end{bmatrix} \begin{bmatrix} 1 \\ \Delta b' \\ \Delta b'^2 \\ \Delta b'^3 \end{bmatrix} = \{P_1\}^T[K]\{P_2\}. \quad (34)$$

Considering the selection of 3×2 order polynomial fitting, the residual error after correction is less than ± 6 nm, as shown in Figs. 11(a) and 11(b), which satisfies the requirement of active optics (AO).

B. Simulation Results

In order to verify the feasibility of the model, we establish the FEA model of the SSA for simulation analysis, shown as Fig. 12.

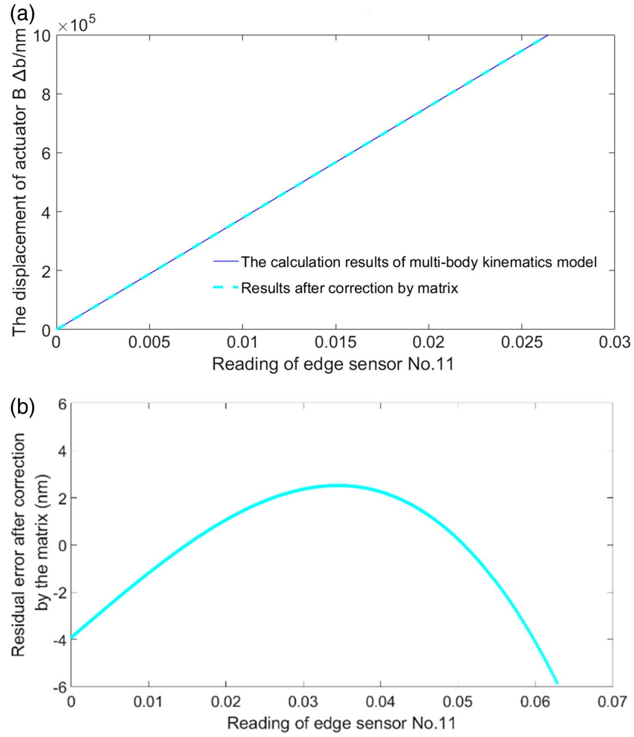

Fig. 11. Residual of 3×2 order polynomial fitting is less than 6 nm: (a) Displacement of actuator B. (b) Residual error after correction by the matrix.

We used HYPERMESH, ANSYS, and MATLAB for a joint simulation analysis to get the results shown in Fig. 13. In this paper, we have established two analytical modes, A and B. Model A is theoretical model in which parts other than the guide flexure are treated as absolute rigid body. As a control group, Model B is an actual model in which all parts are given real material properties.

The blue line represents the calculation results of the theoretical model, the green line represents the simulation results of the theoretical model (Model A), and the red line represents the simulation results of the actual model (Model B).

We can get the following results from Fig. 13:

- The simulation results of the theoretical model (green line) and the calculation results of the theoretical model (blue

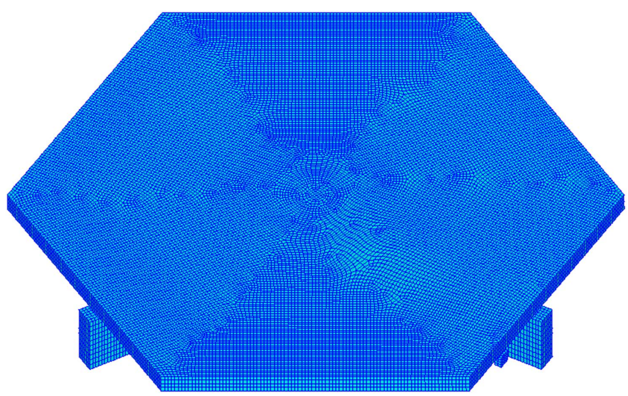

Fig. 12. Finite element model of SSA.

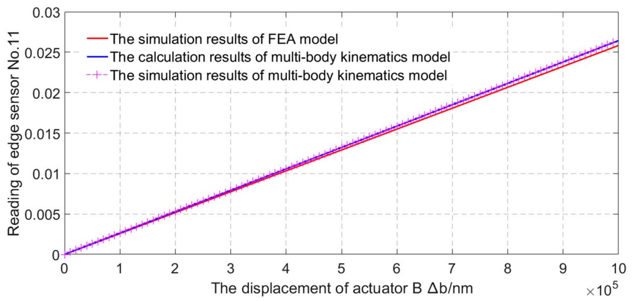

Fig. 13. Comparison of theoretical results with simulation results.

line) are perfectly consistent, and this illustrates the feasibility of the equivalent model.

- The simulation results of the theoretical model (Model A) are generally consistent with the results of the actual model (Model B), but there is still a slight deviation. As the output value of the actuator increases, the deviation increases linearly, which is due to the cumulative deformation error of the SSA increasing with the output value of the actuator increasing. It will not be treated as an absolute rigid body when the error accumulates to a certain value.
- The deformation cumulative error of SSA increases linearly with the increase of the output value of the actuator, which facilitates the subsequent correction.

In this paper, we introduce the 5 × 3 order polynomial for error correction as shown in Fig. 14, and the modified relative error is less than 0.01%.

Residuals of the readings of the edge sensor after being corrected by the 5 × 3 order polynomial are shown in Fig. 15. The absolute value of the residual error of the measurement is less than ±1 nm on full range, which meets the requirements of active optics.

The reasons for the structural errors are summarized as follows:

- The material properties of the SSA.
- The geometric size of the SSA.
- The constraints of the location of the SSA.
- The effects of ambient temperature.
- The effects of the structural vibration.
- Other factors.

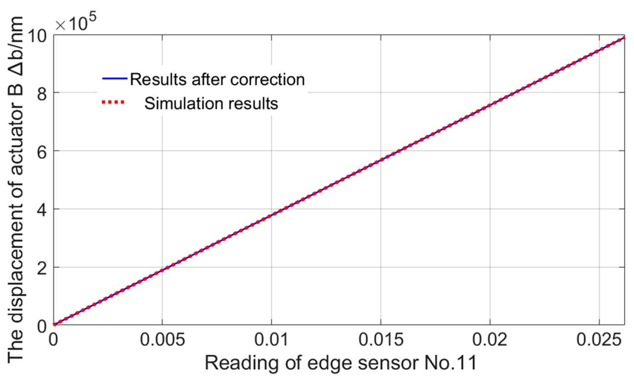

Fig. 14. Actual values and theoretical values of edge sensor's readings after corrected by 5 × 3 order polynomial.

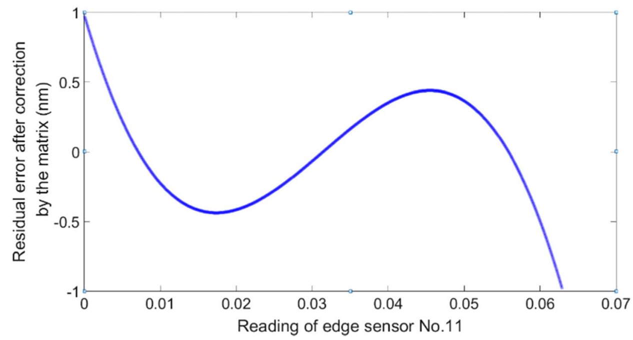

Fig. 15. Residuals of the readings of edge sensor after being corrected by 5 × 3 order polynomial.

5. ANALYSIS OF THE INFLUENCE OF TIP AND TILT ON THE READING OF THE EDGE SENSORS

As shown in Fig. 16, as the angle of tilt θ decreases, the edge sensor's curve moves down, but the reading is still

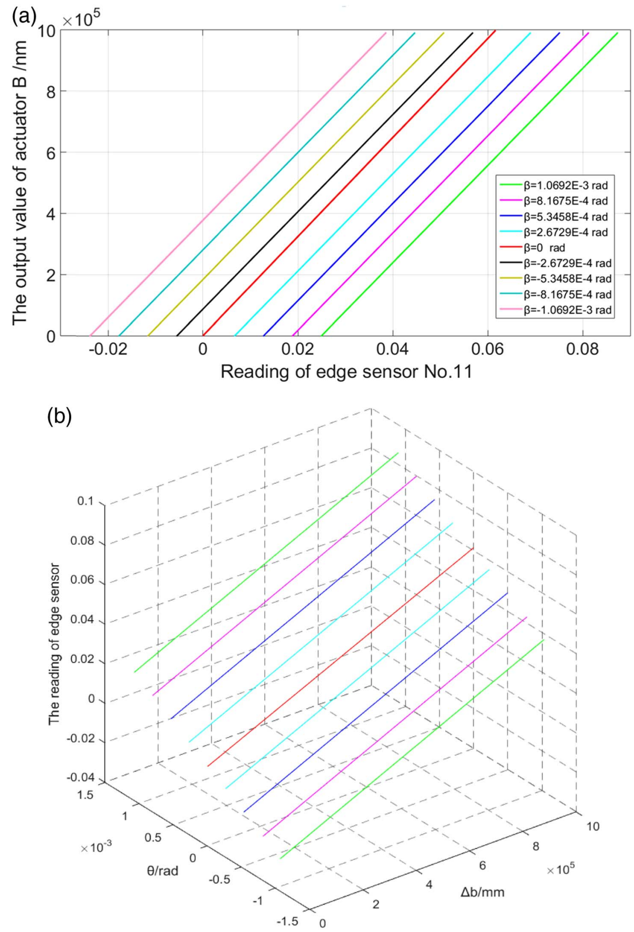

Fig. 16. Influence of tilt on the reading of the edge sensor: (a) Relationship between the reading of edge sensor No. 11 and the output value of actuator B at different tilt angles in the 2D view; β is the angle of tilt. (b) Relationship between the reading of edge sensor No. 11 and the output value of actuator B at different tilt angles in the 3D view; Δb is the output value of actuator B, and θ is the angle of tilt.

approximately linear with the output value of the actuator increasing when θ is constant:

$$\Delta b = [1 \quad \Delta a \quad \Delta a^2 \quad \Delta c \quad \Delta c^2] * \begin{bmatrix} k_{11} & k_{12} & k_{13} \\ k_{21} & k_{22} & k_{23} \\ k_{31} & k_{32} & k_{33} \\ k_{41} & k_{42} & k_{43} \\ k_{51} & k_{52} & k_{53} \end{bmatrix} \begin{bmatrix} 1 \\ \Delta b' \\ \Delta b'^2 \end{bmatrix} + \varphi(\theta), \qquad (35)$$

where $\varphi(\theta)$ is a linear function of θ, which is given by

$$\tan \theta = \sqrt{3}(\Delta a - \Delta c)/3l. \qquad (36)$$

Given that θ is a small amount, $\varphi(\theta)$ can be computed in a simplified Eq. (37):

$$\varphi(\theta) \approx \varphi(\tan \theta) = \psi(\Delta a - \Delta c). \qquad (37)$$

We assume that $\psi(\Delta a - \Delta c) = k_0(\Delta a - \Delta c) + b_0$ and Eq. (35) is converted to

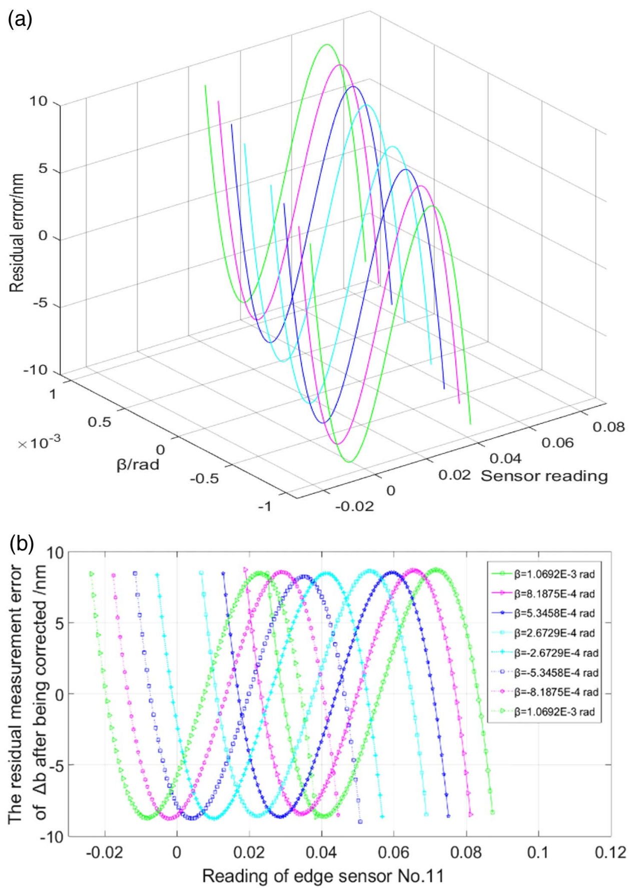

Fig. 17. Relationship between sensor reading and residual error after being fitted with 5×3 order polynomial. (The absolute value of residual error is less than 4.5 nm RMS.) (a) 3D view of the residual measurement error of Δb after being corrected. (b) 2D view of the residual measurement error of Δb after being corrected.

$$\Delta b = [1 \quad \Delta a \quad \Delta a^2 \quad \Delta c \quad \Delta c^2] * \begin{bmatrix} k_{11} + b_0 & k_{12} & k_{13} \\ k_{21} + k_0 & k_{22} & k_{23} \\ k_{31} & k_{32} & k_{33} \\ k_{41} - k_0 & k_{42} & k_{43} \\ k_{51} & k_{52} & k_{53} \end{bmatrix} \begin{bmatrix} 1 \\ \Delta b' \\ \Delta b'^2 \end{bmatrix}. \qquad (38)$$

6. CONCLUSION

This paper introduces a class of edge sensors that are used in the TMT baseline. The measured value of the edge sensor and relative pose of adjacent segmented mirrors are formulated by using the capacitor theorem and the homogeneous transformation method. Based on the multi-body kinematics theorem, we present a simplified kinematics model of single segmented mirror. The simulation results indicate that the theoretical results are in good agreement with the simulation results and this model can effectively reflect the segment's actual movement process in the presence of deformation of the guide flexure. When the travel range of every actuator is limited within ± 1 mm, the maximum linear error of this model is less than 5.86×10^{-6}. Besides, a matrix function is defined and formulated to correct the measurement error of the edge sensor that is generated by the deformation of the guide flexure. The results show that this method can effectively suppress the measurement error introduced by the deformation of the guide flexure and improve the utilization of readings while guaranteeing the accuracy of the measured values. The absolute value of error is less than 4.5 nm, as shown in Fig. 17, in the whole measurement range and meets the requirement (5 nm) [29].

Funding. Youth Innovation Promotion Association of the Chinese Academy of Sciences (CAS) (2016198); National Natural Science Foundation of China (NSFC) (11403022, 11673080).

Acknowledgment. The authors are very grateful to the TMT group for their technology support.

REFERENCES

1. H. S. Zhao, X. J. Li, B. Fan, and Z. G. Zeng, "Deformation verification and surface improvement of active stressed lap for 4 m-class primary mirror fabrication," Appl. Opt. **54**, 2658–2664 (2015).
2. B. Sedghi, M. Müller, and M. Dimmler, "Analyzing the impact of vibrations on E-ELT primary segmented mirror," Proc. SPIE **9911**, 991111 (2016).
3. D. G. MacMynowski, K. Vogiatzis, G. Z. Angeli, J. Fitzsimmons, and J. E. Nelson, "Wind loads on ground-based telescopes," Appl. Opt. **45**, 7912–7913 (2006).
4. S. Tichkule and A. Muschinski, "Effects of wind-driven telescope vibrations on measurements of turbulent angle-of-arrival fluctuations," Appl. Opt. **53**, 4651–4660 (2014).
5. G. J. Hill, N. Drory, J. M. Good, H. Lee, B. L. Vattiat, H. Kriel, J. Ramsey, R. Bryant, L. Elliot, J. Fowler, M. Häuser, M. Landiau, R. Leck, S. Odewahn, D. Perry, R. Savage, E. S. Mrozinski, M. Shetrone, D. L. DePoy, T. Prochaska, J. L. Marshall, G. Damm, K. Gebhardt, P. J. MacQueen, J. Martin, T. Armandroff, and L. W. Ramsey, "Deployment of the Hobby-Eberly Telescope wide field upgrade," Proc. SPIE **9906**, 990606 (2016).

6. X. Y. Liu, J. X. Zhang, X. X. Wu, J. F. Li, P. Guo, and Q. C. An, "Study on the sensitivity of temperature gradient for large aperture SiC lightweight mirror based on active optics," Proc. SPIE **9980**, 99800I (2014).
7. A. Rakich, "A primary mirror metrology system for the GMT," Proc. SPIE **9906**, 99062O (2016).
8. F. Shi, B. M. King, N. Sigrist, and S. A. Basinger, "NIRCam long wavelength channel grisms as the dispersed fringe sensor for JWST segment mirror coarse phasing," Proc. SPIE **7010**, 70102E (2008).
9. X. Q. Cui, Y. H. Zhao, and Y. Q. Chu, "The large sky area multi-object fiber spectroscopic telescope (LAMOST)," Res. Astron. Astrophys. **12**, 1197–1242 (2012).
10. P. Palunas, J. R. Fowler, J. A. Booth, G. Damm, and G. H. Ames, "Control of the Hobby-Eberly telescope primary mirror array with the segment alignment maintenance system," Proc. SPIE **5496**, 659–662 (2004).
11. B. Lefort and J. Castro, "The GTC primary mirror control system," Proc. SPIE **7019**, 70190I (2008).
12. C. Hull, S. Gunnels, M. Johns, J. Kern, A. Talmor, M. Ward, and S. Shectman, "Giant Magellan telescope primary mirror cells," Proc. SPIE **7733**, 773327 (2010).
13. T. S. Mast, G. Gabor, and J. E. Nelson, "Edge sensors for a segmented mirror," Proc. SPIE **444**, 297–309 (1983).
14. H. Gajjar, J. Menzies, D. Buckley, C. Coetzee, D. Bester, O. Strydom, J. Love, and K. Browne, "SALT: active control of the primary mirror with inductive edge sensors," Proc. SPIE **9906**, 990639 (2016).
15. H. Gajjar, J. Menzies, D. Buckley, C. Neel, P. Parbaud, and S. Royet, "SALT segmented primary mirror: inductive edge sensors," Proc. SPIE **9145**, 91454X (2014).
16. Y. Zhang, D. H. Yang, and X. Q. Cui, "Measuring seeing with a Shack-Hartmann wave-front sensor during an active-optics experiment," Appl. Opt. **43**, 729–732 (2004).
17. T. Mast, G. Chanan, J. Nelson, R. Minor, and R. Jared, "Edge sensor design for the TMT," Proc. SPIE **6267**, 62672S (2006).
18. M. Wasmeier, J. Hackl, and S. Leveque, "Inductive sensors based on embedded coil technology for nanometric inter-segment position sensing of the E-ELT," Proc. SPIE **9145**, 91451R (2014).
19. E. C. Williams, C. Baffes, T. Mast, J. Nelson, B. Platt, R. J. Ponchione, E. Ponslet, S. Setoodeh, M. Sirota, V. Stephens, L. Stepp, and A. Tubb, "Advancement of the segment support system for the thirty meter telescope primary mirror," Proc. SPIE **7018**, 701810 (2008).
20. D. G. MacMynowski, P. M. Thompson, and M. J. Sirota, "Analysis of TMT primary mirror control-structure interaction," Proc. SPIE **7017**, 701715 (2008).
21. T. Mast and J. Nelson, "TMT primary mirror segment shape," Technical Report TMT.OPT.TEC.04.001.REL01 (2004).
22. J. Nelson, T. Mast, and G. Chanan, "Segmented mirror telescopes," in *Planets, Stars and Stellar Systems*, T. D. Oswalt and I. S. Mclean, eds. (Academic, 2011), pp. 107–115.
23. R. H. Minor, A. A. Arthur, G. Gabor, H. G. Jackson, R. C. Jared, T. S. Mast, and B. A. Schaefer, "Displacement sensors for the primary mirror of the W. M. Keck telescope," Proc. SPIE **1236**, 1009–1017 (1990).
24. K. Brindley, "Capacitors," in *Starting Electronics* (Academic, 2011), pp. 71–73.
25. X. N. Li, Z. B. Jiang, X. F. Gong, H. Y. Zhang, K. X. Chen, Y. Zheng, B. Li, B. B. Yu, C. Xu, B. Ji, and Q. Y. Xu, "Stressed mirror annular polishing for scale-down TMT primary segments," Proc. SPIE **9912**, 99120A (2016).
26. C. Weiland, "Coordinate transformations," in *Computational Space Flight Mechanics* (Academic, 2010), pp. 7–23.
27. C. Weiland, "Transformations between often used coordinate systems," in *Computational Space Flight Mechanics* (Academic, 2010), pp. 25–30.
28. G. Chanan, J. Nelson, C. Ohara, and E. Sirko, "Design issues for the active control system of the California extremely large telescope (CELT)," Proc. SPIE **4004**, 363–372 (2000).
29. C. Shelton, M1CS Sensor System Preliminary Design Review, document archive Docushare TMT.CTR.PRE.12.017.REL01 (March 2005).